

Resolution analysis of magnetically arrested disk simulations

L. Salas¹★ G. Musoke^{2,1} K. Chatterjee^{3,4} S.B. Markoff^{1,5} O. Porth¹ M.T.P. Liska^{6,7} B. Ripperda^{2,8–11}

¹*Anton Pannekoek Institute for Astronomy, University of Amsterdam, Science Park 904, 1098 XH Amsterdam, The Netherlands*

²*Canadian Institute for Theoretical Astrophysics, University of Toronto, 60 St. George Street, Toronto, ON M5S 3H8, Canada*

³*Institute for Research in Electronics and Applied Physics, University of Maryland, 8279 Paint Branch Drive, College Park, MD 20742, USA*

⁴*Black Hole Initiative at Harvard University, 20 Garden Street, Cambridge, MA 02138, USA*

⁵*Gravitation and Astroparticle Physics Amsterdam Institute, University of Amsterdam, Science Park 904, 1098 XH 195 196 Amsterdam, The Netherlands*

⁶*Center for Relativistic Astrophysics, Georgia Institute of Technology, Howey Physics Bldg, 837 State St NW, Atlanta, GA, 30332, USA*

⁷*Institute for Theory and Computation, Harvard University, 60 Garden Street, Cambridge, MA 02138, USA*

⁸*Dunlap Institute for Astronomy and Astrophysics, University of Toronto, 50 St. George Street, Toronto, ON M5S 3H4, Canada*

⁹*Department of Physics, University of Toronto, 60 St. George Street, Toronto, ON M5S 1A7, Canada*

¹⁰*Perimeter Institute for Theoretical Physics, 31 Caroline Street North, Waterloo, ON N2L 2Y5, Canada*

¹¹*Center for Computational Astrophysics, Flatiron Institute, 162 5th avenue, New York, NY, 10010, USA*

Accepted 2024 July 25. Received 2024 July 19; in original form 2024 April 19

ABSTRACT

Polarisation measurements by the Event Horizon Telescope from M87* and Sgr A* suggest that there is a dynamically strong, ordered magnetic field, typical of what is expected of a magnetically arrested accretion disk (MAD). In such disks the strong poloidal magnetic field can suppress the accretion flow and cause episodic flux eruptions. Recent work shows that General Relativistic Magnetohydrodynamic (GRMHD) MAD simulations feature dynamics of turbulence and mixing instabilities that are becoming resolved at higher resolutions. We perform a convergence study of MAD states exceeding the status quo by an order of magnitude in resolution. We use existing 3D simulations performed with the H-AMR code, up to resolution of $5376 \times 2304 \times 2304$ in a logarithmic spherical-polar grid. We find consistent time-averaged disk properties across all resolutions. However, higher resolutions reveal signs of inward angular momentum transport attributed to turbulent convection, particularly evident when mixing instabilities occur at the surfaces of flux tubes during flux eruptions. Additionally, we see wave-like features in the jet sheath, which become more prominent at higher resolutions, that may induce mixing between jet and disk. At higher resolutions, we observe the sheath to be thinner, resulting in increased temperature, reduced magnetisation, and greater variability. Those differences could affect the dissipation of energy, that would eventually result in distinct observable radiative emission from high-resolution simulations. With higher resolutions, we can delve into crucial questions about horizon-scale physics and its impact on the dynamics and emission properties of larger-scale jets.

Key words: accretion, accretion disks – black hole physics – MHD

1 INTRODUCTION

The accretion of matter is a fundamental astrophysical process occurring across a variety of compact objects such as neutron stars, white dwarfs, and black holes (BHs). Jets and wind outflows are a natural consequence of the accretion process and are present across all scales of black hole mass— from black hole X-ray binaries to the supermassive black holes powering the bright compact regions at the centres of most massive galaxies (active galactic nuclei; AGN). Accretion disks and outflows emit radiation across the electromagnetic spectrum, from radio frequencies to high energy gamma rays (e.g. EHTC MWL M87*2017; EHTC Sgr A*2017 II). The relativistic outflows (jets) launched by AGN in particular are thought to have a profound effect on their environments, playing a key role in regulating star formation, galaxy evolution and the evolution of galaxy clusters (e.g. Silk & Rees 1998; Schawinski et al. 2007; Fabian 2012).

Numerical simulations have improved our understanding of the accretion process and the mechanisms by which jets are launched and affect their environments. Yet it remains unclear which resolutions are sufficient to accurately capture the global evolution of accreting black holes, and jets.

Theoretical modelling and numerical simulations, combined with multi-wavelength observations have provided critical insights into the nature of outflows (jets) and radiation from accreting black hole systems (e.g. Yuan & Narayan 2014; EHTC M87*2017 I; EHTC Sgr A*2017 I). In particular, GRMHD simulations have become increasingly successful in explaining the dynamics of the accretion flow, winds, and the evolution of relativistic jets close to the black hole, therefore playing a fundamental role in the interpretation of observational data. GRMHD simulations have been significantly improving over the last few decades owing to the increase in computing power and the development of efficient numerical algorithms in multiple GRMHD codes (e.g. Athena++; K-ATHENA; BHAC; COSMOS++; ECHO; H-AMR; KHARMA; IllinoisGRMHD; KORAL;

★ E-mail: l.d.sosapantasalas@uva.nl

Uwabami). Porth et al. (2019) demonstrated the general robustness of GRMHD simulation results regardless of the different algorithms, implementations, and grid geometries of different numerical codes in the weakly magnetized regime (SANE). Recently, there has been significantly more interest in a category of numerical solutions wherein strong poloidal magnetic fields can interrupt the accretion flow, forming a magnetically arrested disk (MAD; Bisnovatyi-Kogan & Ruzmaikin 1974; Narayan et al. 2003). White et al. (2019) conducted a resolution study of MAD accretion flows, with a maximum effective 173 cells per decade in radius, 256 cells in polar angle and 512 cells in azimuthal angle. They showed that the general large-scale structure of the flow is robust with resolution. However, the spatial structure and Lorentz factor of the jet were not fully converged.

In recent years, the unprecedented resolution of the Event Horizon Telescope (EHT) has enabled the first direct imaging of the plasma surrounding the supermassive black holes M87* and Sgr A* (EHTC M87*2017 I; EHTC Sgr A*2017 I). The EHT observations revealed a bright ring, formed by the hot luminous plasma close to the black hole, along with a dark central region, the black hole ‘shadow’. Synthetic images produced by ray-tracing of GRMHD simulations are the fiducial models used by the EHT collaboration to compare against observations. The closest-matching GRMHD simulations to the EHT observations suggest that both M87* and Sgr A* exhibit accretion flows in the MAD regime (e.g. EHTC M87*2017 V; EHTC M87*2017 VIII; EHTC M87*2017 IX; EHTC Sgr A*2017 V). Moreover, Sgr A* can reach the MAD state in the inner region when poloidal magnetic fields are advected inwards from larger scales, as demonstrated by wind-fed accretion simulations (Ressler et al. 2023). Additionally, Liska et al. (2020) showcased that turbulence within the accretion disk itself can generate strong poloidal magnetic fields in-situ.

Recent work shows that MAD states feature complicated dynamics that become resolved at higher resolutions. Consequently, simulating MAD states is numerically challenging. Episodic flux eruptions result in the ejection of large cavities containing flux tubes with low-density through magnetic reconnection (Ripperda et al. 2020, 2022), which may serve as a mechanism for flare generation (Dexter et al. 2020; Porth et al. 2021; Ripperda et al. 2022; Hakobyan et al. 2023). The Rayleigh-Taylor instability (RTI) mechanism acting on the boundary of a flux tube can lead to secondary instabilities, turbulence, and magnetic reconnection (Zhdankin et al. 2023). Ripperda et al. (2022) captured plasmoid-mediated magnetic reconnection in a 3D MAD state for the first time, by conducting a GRMHD simulation with maximum effective resolution of 1630 cells per decade in radius, 2304 cells in polar angle and 2304 cells in azimuthal angle. Plasmoid-mediated magnetic reconnection can result in particle energisation through dissipation and may explain flares from accreting black holes, in particular the TeV flares observed from M87* (Aharonian et al. 2006; Acciari et al. 2010; Aliu et al. 2012; Blanch 2021), and the infrared and X-ray flares thought to originate close to the event horizon of Sgr A* (Baganoff et al. 2001; Eckart et al. 2004; Neilsen et al. 2015; GRAVITY Collaboration et al. 2018; Gravity Collaboration et al. 2021).

The current simulations conducted with the Graphics Processing Unit (GPU)-accelerated GRMHD code H-AMR (Liska et al. 2022) are pushing the boundaries of what is computationally feasible with regards to resolution. However, conducting high resolution GRMHD simulations is computationally extremely expensive. In this paper, we perform a convergence study on a wider range of resolutions than has ever been previously explored (see Table 1), employing existing 3D ideal GRMHD simulations with H-AMR of an accreting black hole in the MAD regime (Ripperda et al. 2022). We determine

how well the physical properties of the accretion flow at different spatial resolutions agree. We identify the processes that are only recovered at high resolutions. We constrain the minimum resolution that ensures consistent and converged results, which will enable the GRMHD community to minimise the computational cost of these simulations, without sacrificing the accuracy of the global evolution of the disk-jet-black hole system.

The structure of this paper is as follows: Section 2 provides the numerical setup for simulations and an overview of the H-AMR code. The impact of resolution on the disk and the jet is analysed in Section 3. The conclusions of the study are presented in Section 4.

2 SIMULATIONS

2.1 GRMHD equations

The equations of GRMHD comprise the particle number conservation equation:

$$(nu^\mu)_{;\mu} = 0, \quad (1)$$

the energy momentum conservation equations:

$$T^\mu{}_{\nu;\mu} = 0, \quad (2)$$

and the Maxwell’s equations:

$$F^{*\mu\nu}{}_{;\nu} = 0, \quad (3)$$

In ideal MHD, the dual of the electromagnetic field tensor is $F^{*\mu\nu} = b^\mu u^\nu - b^\nu u^\mu$ and the stress-energy tensor is:

$$T^\mu{}_{\nu} \equiv (\rho + u_g + p_g + b^2) u^\mu u_\nu - b^\mu b_\nu + \left(\frac{1}{2} b^2 + p_g\right) \delta^\mu{}_{\nu}, \quad (4)$$

Here n is the particle number density, $\rho = mn$ is the rest mass density¹, m is the mean rest mass per particle, u_g is the gas energy density, p_g is the gas pressure, and $b^2/2$ is the magnetic energy density. The 4-velocity and the magnetic field 4-vector are u^μ and b^μ respectively. $\delta^\mu{}_{\nu}$ is the Kronecker delta. The gas pressure is proportional to the fluid-frame rest-mass density and proton temperature ($p_g \propto \rho T_p$) and the magnetic pressure $p_b = b^2/2$, where b is the magnetic field strength in the frame co-moving with the fluid. The proton temperature (T_p), in CGS units:

$$T_p = \frac{m_p c^2 p_g}{k_B \rho}, \quad (5)$$

where m_p is the proton mass and k_B is the Boltzmann constant. We use geometrized units with gravitational constant, black hole mass, and speed of light $G = M = c = 1$, and a factor of $1/\sqrt{4\pi}$ is absorbed in the definition of the magnetic field. Greek indices run through $[0, 1, 2, 3]$ and Roman indices through $[1, 2, 3]$. The metric determinant is g .

2.2 H-AMR implementation

H-AMR (Liska et al. 2022), a state-of-the-art 3D GRMHD code, builds upon the foundation of the original HARM2D code (Gammie et al. 2003). H-AMR converts conserved quantities, such as particle number density and energy-momentum density, into primitive variables, including rest-mass density, internal energy density, and velocity components, utilising the inversion scheme by Noble et al. (2006).

¹ Normalised to a maximum density $\rho_{\max} = 1$.

The Adaptive mesh refinement (AMR), local adaptive time-stepping (LAT), and GPU acceleration within a hybrid CUDA-OpenMP-MPI framework utilised in H-AMR speed-up computations. The achieved resolutions are $\approx 10 \times 10 \times 5$ times higher than those in the previous MAD study (White et al. 2019).

H-AMR utilises a staggered grid for constrained transport of magnetic fields as described in (Gardiner & Stone 2005), and solves the GRMHD equations of motion in conservative form in arbitrary (fixed) spacetimes. H-AMR uses a finite volume, shock-capturing Godunov-based HLLC scheme, with third order accurate spatial reconstruction of cell variables (PPM, Colella & Woodward 1984) on cell faces and second order accurate time evolution. The simulations are performed on a logarithmic spherical-polar grid in a Kerr-Schild foliation, $\log(r)$, θ and ϕ . Since cells get squeezed near the pole, the timestep in all spherical grids is reduced by an additional factor proportional to the resolution in the ϕ -direction. To remedy this issue, multiple levels of static mesh de-refinement in the ϕ -direction are used to keep the aspect ratio of the cells close to uniform at high latitudes. This method prevents the squeezing of cells near the pole from reducing the global timestep, while maintaining high accuracy in all three dimensions (see section 3.4 in Liska et al. 2022). The simulations presented in this work utilise outflow boundary conditions in the radial direction, transmissive boundary conditions in the θ -direction and periodic boundary conditions in the ϕ -direction.

2.3 Numerical setup

In order to study convergence in GRMHD simulations of MAD accretion flows around a spinning black hole, we analyse a total of five 3D GRMHD simulations. The simulation with the highest resolution, R5, is performed with an effective² resolution of $5376 \times 2304 \times 2304$ and the other four simulations we present are a factor $\approx 2 \times 2 \times 2$ less in resolution (see Table 1). The radial domain of the simulation grid is $r = [1.2 - 2000] r_g$. Each simulation is evolved for at least $10^4 r_g/c$ (see fifth column of Table 1). In all runs the disk is initialised using a torus in hydrostatic equilibrium (Fishbone & Moncrief 1976) around a Kerr black hole with dimensionless spin $a = 0.9375$. The inner edge of the torus is located at $r = 20 r_g$ and the pressure maximum at $r = 41 r_g$. The torus is threaded with a single poloidal magnetic field loop, defined by the ϕ -component of the vector potential $A_\phi \propto \max[\rho/\rho_{\max} (r/r_{\text{in}})^3 \sin^3 \theta \exp(-r/400) - 0.2, 0]$, and normalised to obtain a gas-to-magnetic-pressure ratio $p_{g,\text{max}}/p_{b,\text{max}} = 100$. We adopt an equation of state for an ideal gas with an adiabatic index of $\gamma_{\text{ad}} = 13/9$, which corresponds approximately to a gas mixture of relativistic electrons $\gamma_{\text{ad},e} = 4/3$ and non-relativistic ions $\gamma_{\text{ad},p} = 5/3$. A semi-relativistic gas with $\gamma_{\text{ad}} \sim 1.55$ was found for BH accreting at $\sim 10^{-6}$ the Eddington accretion rate, in radiative two-temperature GRMHD simulations (Liska et al. 2024). Within the spine region the following floor and ceiling values are employed; the rest-mass density floor is $\rho_{\text{fl}} = \text{MAX}[b^2/25, 10^{-7} r^{-2}, 10^{-20}]$, the gas energy density floor is $u_{g,\text{fl}} = \text{MAX}[b^2/750, 10^{-9} r^{-26/9}, 10^{-20}]$ and the magnetisation ceiling is $\sigma_{\text{max}} = 25$ where $\sigma = b^2/\rho$. The disk is initialised with the same energy density perturbation for all resolutions, $u_g(1 + 0.04(\text{rand}([0, 1]) - 0.5))$, where $\text{rand}([0, 1])$ is a random deviate between 0 and 1.

² To prevent the squeezing of cells, three internal and four external derefinement levels in ϕ are used to reduce the resolution from $N_\phi = 128 - 2304$ at $30^\circ < \theta < 150^\circ$ to $N_\phi = 16 - 18$ within $0.5^\circ - 7.5^\circ$ of each pole (Liska et al. 2022).

Table 1. Number of cells in the radial N_r , polar N_θ and azimuth N_ϕ directions for each simulation, together with the final time of the simulation t_{sim} .

Resolution	N_r	N_θ	N_ϕ	$t_{\text{sim}}(r_g/c)$
R1	288	128	128	20420
R2	580	288	256	22790
R3	1280	576	512	12330
R4	2240	1056	1024	10780
R5	5376	2304	2304	10000

3 RESULTS

There are various definitions of jets and unbound outflows in the literature (see e.g. Narayan et al. 2012; Yuan et al. 2015). One option to define the jet region is by using $(-T^r_t/(\rho u^r))^2 - 1 > 1$, where $-T^r_t$ is the radial ($\mu = 1$)-temporal ($\nu = 0$) component of the stress-energy tensor (Equation 4), representing the outward radial energy flux. This is equivalent to the region where the total energy per unit rest-mass is greater than $\sqrt{5}c^2$ (EHTC M87*2017 V; EHTC M87*2017 VIII). Alternatively the jet region can also be defined as in Mościbrodzka & Falcke (2013), where the jet is taken to be the unbound gas outflowing with a minimum bulk velocity $v_{\text{min}}/c = 0.2$ as measured in a normal observer frame, and the jet spine is taken to be the region at which $\sigma > 0.1$. In this paper, we follow the definitions in Davelaar et al. (2018) in Kerr-Schild coordinates, where the jet is characterised by two components: (1) The jet spine– a relativistic and strongly magnetized outflow ($\sigma > 1$). (2) The jet sheath– a mildly relativistic outflow defined using the Bernoulli parameter $Be = -\tilde{h}u_t > 1.02$ where $\tilde{h} = (\rho + u_g + p_g)/\rho$ is the specific gas enthalpy and u_t is the time component of the inverse four-velocity.

For a qualitative perspective, Fig. 1 shows 2D slices through azimuthal angle $\phi = 0$ for density ρ , proton temperature T_p , and magnetisation $\sigma = b^2/\rho$ for the simulations conducted at different resolutions. As the simulation resolution increases, wave-like features in the jet sheath become more prominent and plasmoids in current sheets close to the event horizon are captured for resolution R5. Additionally, the jet sheath gets hotter and less magnetised.

3.1 Disk properties

In order to determine quantitative differences between the simulations we compare various fluid parameters, as defined in the following subsections. The averaged profile of a variable X is calculated by integrating over θ and ϕ with a combination of three conditions to select the disk; the disk is taken to be the region that satisfies density $\rho/\rho_{\text{max}} = \rho > 10^{-4}$, magnetisation $\sigma < 1$ and Bernoulli parameter $Be < 1.02$. Additionally, we include a density weight to give more relevance to regions of the disk with higher density.³

$$\langle X \rangle_{\rho[\theta, \phi]}^{\text{disk}} = \frac{\iint X \rho \left(\rho > 10^{-4} \right) (\sigma < 1) (Be < 1.02) \sqrt{-g} d\theta d\phi}{\iint \rho \left(\rho > 10^{-4} \right) (\sigma < 1) (Be < 1.02) \sqrt{-g} d\theta d\phi}. \quad (6)$$

3.1.1 Fluxes

In this section we determine the impact of resolution on the temporal evolution of the mass, magnetic and energy fluxes in the simulations.

³ Note the difference in notation, $\langle \rangle$ without any sub/super script is time average.

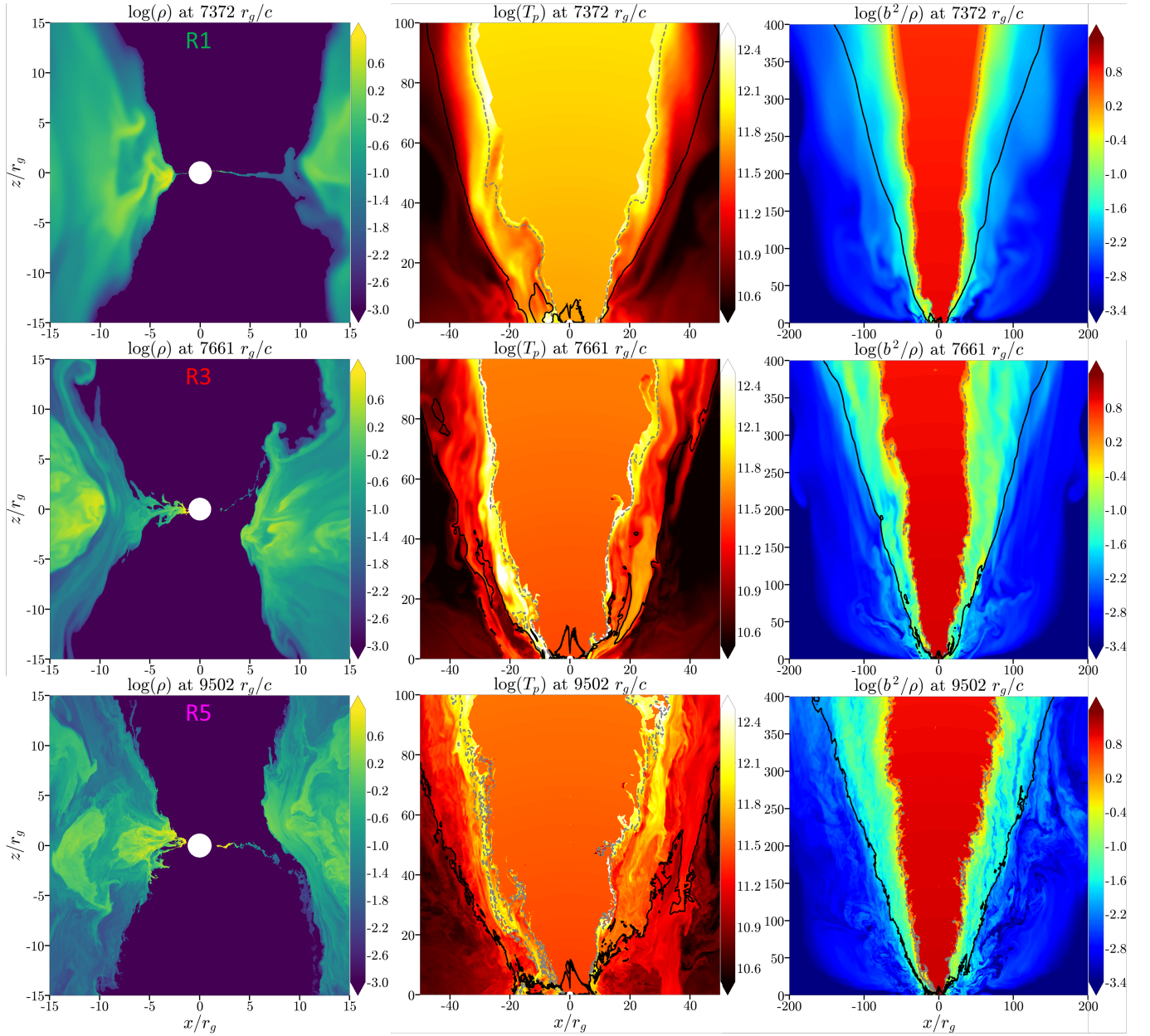


Figure 1. Meridional 2D slices through $\phi = 0$ for (log) density ρ (left column), proton temperature T_p in Kelvin (middle column), and magnetisation $\sigma = b^2/\rho$ (right column) during a flux eruption event, when the normalised magnetic flux on the event horizon φ_{BH} approaches a local minimum (Fig. 3). From top to bottom: resolution R1, R3 and R5. The grey dashed and black lines correspond to surfaces where $\sigma = 1$ and $Be = 1.02$, respectively. The jet has two components: the spine (defined as the region in which $\sigma > 1$) and the sheath (defined as the region in which $\sigma < 1$ and $Be > 1.02$). The dominance of numerical floors undermines the reliability of the jet spine. We partially cover the spine with a zero screen for the plot of ρ and time-average screens for T_p and σ . These screens are activated for $\sigma > 3$, allowing visibility of plasma within the range of $1 < \sigma < 3$.

The fluxes are defined as follows⁴. The mass accretion rate \dot{M} is given by:

$$\dot{M} \equiv - \iint \rho u^r \sqrt{-g} d\theta d\phi. \quad (7)$$

\dot{M}_{BH} is contaminated by artificial matter injection due to density floors above and below the black hole poles up to a radius of \approx

⁴ Subscripts indicate where in the radial domain the fluxes are analysed, e.g. \dot{M}_{BH} at the event horizon and \dot{M}_{5r_g} at $5r_g$.

$5r_g$. Therefore, \dot{M}_{5r_g} is a better representation of the real accretion process. The energy flux \dot{E} is given by:

$$\dot{E} \equiv - \iint T^r_t \sqrt{-g} d\theta d\phi. \quad (8)$$

The energy outflow efficiency of the jet spine is the energy return rate divided by the time averaged mass accretion rate:

$$\eta_j \equiv \frac{\dot{M} - \dot{E}_{spine}}{\langle \dot{M} \rangle}. \quad (9)$$

To calculate the energy flux in the jet spine only \dot{E}_{spine} , we add an extra condition before doing the integral, which is the magnetisation greater than 1 ($\sigma > 1$). The magnetic flux is defined as:

$$\Phi \equiv \frac{1}{2} \iint |B^r| \sqrt{-g} d\theta d\phi. \quad (10)$$

To study MAD simulations is convenient to use the normalised magnetic flux:

$$\varphi \equiv \frac{\Phi}{\sqrt{\langle \dot{M} \rangle}}, \quad (11)$$

known as the ‘‘MAD parameter’’ which, for spin $a = 0.9375$ and torus scale height $H/R \approx 0.3$, has the critical value $\varphi_{\text{max}} \approx 15$ (within the units adopted here; Tchekhovskoy et al. (2012)). H and R are the full height and cylindrical radius of the disk, respectively.

Space-time diagrams of the mass accretion rate (Equation 7) and normalised magnetic flux (Equation 11) are presented in Fig. 2 for the five resolutions of Table 1. A quasi-stationary state of the mass flux is obtained after $t = 5 \times 10^3 r_g/c$ until a radius of around $50r_g$. For $r \approx 50r_g$, there is a balance between inflow and outflow so $\langle \dot{M}_{50r_g} \rangle_{[5-10] \times 10^3 r_g/c} \approx 0$, that marks the point where the torus begins to spread outwards due to viscosity. The relativistic jet and outflows launched from the inner disk have short dynamical timescales. At $\approx 80r_g$, the negative \dot{M} is predominantly due to unbound outflows (spine and sheath). At ≈ 100 and $200r_g$, unbound outflows contribute 50% and 10% of the total \dot{M} , respectively. For example, $\langle \dot{M}_{100r_g} \rangle_{[5-10] \times 10^3 r_g/c} \approx -40$ in code units, with equal contribution from unbound outflows and viscous spreading of the disk. In the analysis of averaged profiles, the properties of the simulations are calculated as time averaged between $t = [8-10] \times 10^3 r_g/c$ to avoid the dependency on the initial conditions for $r > 100r_g$ and $t < 8 \times 10^3 r_g/c$. The disk properties still depend on the initial conditions of the Fishbone-Moncrief torus for radii larger than $40r_g$.

The time evolution of the mass accretion rate \dot{M} at $5r_g$, the normalised magnetic flux φ and the jet outflow efficiency η_j at the event horizon are presented in Fig. 3. The magnetic flux grows until saturation level at around $t = 5 \times 10^3 r_g/c$. The fluctuations are caused by accumulation and escape of field line bundles in the vicinity of the BH. The magnetic pressure of those escaping field lines stops the accretion process for a short time, therefore, a drop in the magnetic flux is correlated to a sudden decrease of the accretion rate. We find that the mass accretion rate decreases with increasing resolution when \dot{M} is computed at a radius of $5r_g$. However, we note that there is no clear tendency for \dot{M} when computed at the horizon— this is due to the artificial matter injection that occurs close to the poles of the BH due to flooring (see Fig. 4 and Table. 2).

The peak, average value and standard deviation of \dot{M} , φ and η_j are presented in Table 2. We use the modulation index MI as a standardised measure of time variability of the accretion rates. It is defined as the ratio of the standard deviation to the mean. In Fig. 4, the MI of \dot{M}_{5r_g} initially decreases from resolution R1 to R3, and from R3 it increases. Similarly, MI of φ_{BH} increases from R2. However, the differences in MI are not statistically significant. The accuracy of the MI calculation is dependent on the length of the simulation time window of analysis, $t = [5-10] \times 10^3 r_g/c$. Longer simulations can provide a more precise measure of the variability. Additionally at higher resolutions, we find greater variability of proton temperature, magnetisation and opening angle of the jet sheath close to the black hole at $\approx 40r_g$ (see Section 3.2). All these differences could affect the predicted multiwavelength spectra, relevant to the EHTC analysis of Sgr A* where the two most promising MAD models show

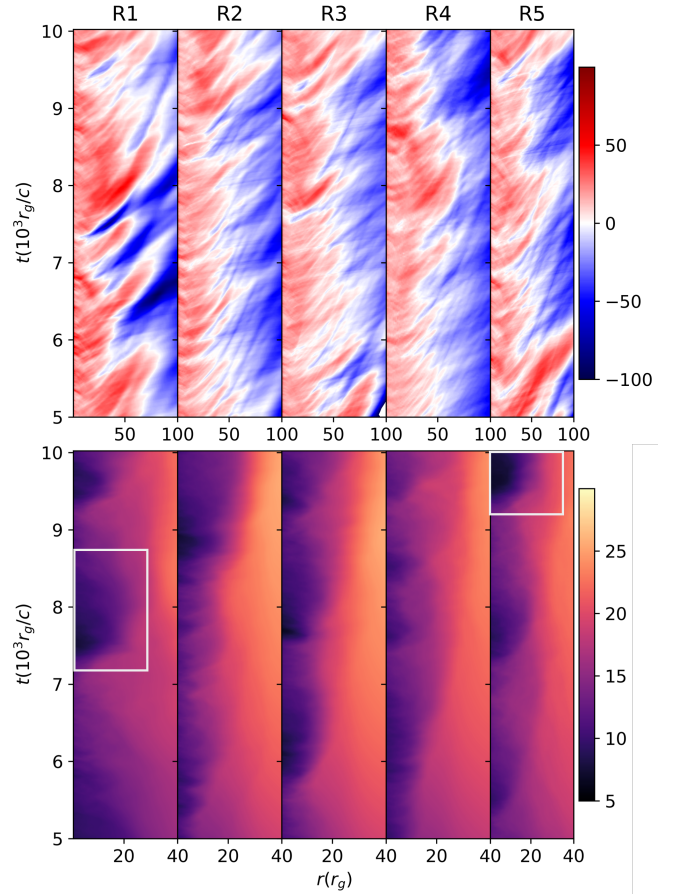


Figure 2. Space-time diagrams of the mass accretion rate (top panel) and normalised magnetic flux (bottom panel). From left to right: resolution R1 to R5. In MAD states, the magnetic flux on the event horizon can build up until it is saturated and gets ejected. In these episodic flux eruption events, the magnetic pressure interrupts the accretion flow, causing flux tubes of low-density material with vertical field to be pushed into the disk until a radius in between 15 and $40r_g$ (e.g. see the white boxes on the bottom panels). Two major eruption events occur for R1, several small eruptions for R2 and R4 and three eruptions for R3 and R5. This behaviour is seen as well in the plot of normalised magnetic flux versus time in the middle panels of Fig. 3.

higher light-curve variability than historical observations at 230 GHz (EHTC Sgr A* 2017 V).

Tchekhovskoy et al. (2011) ran simulations with resolution $288 \times 128 \times \{32, 64, 128\}$, seeded with large poloidal magnetic flux to achieve the MAD state, enabling the production of efficient outflows. The authors demonstrated the extraction of net energy from a spinning black hole’s ergosphere, via the Penrose–Blandford–Znajek mechanism (Blandford & Znajek 1977). The authors found an increase of the average energy outflow efficiency from $\langle \eta_j \rangle \approx 0.30$ to $\approx 1.40 \pm 0.15$ when the BH spin is increased from $a = 0.5$ to 0.99, respectively. McKinney et al. (2012) extended those results by conducting a parametric study of MAD flows with a similar resolution of $272 \times 128 \times 256$ around a rotating black hole with different values of spin, poloidal and toroidal magnetic field geometries. McKinney et al. (2012) confirmed that the Poynting flux outflow is powered by the Blandford-Znajek mechanism when the poloidal magnetic flux saturates near the BH, independently of the initial poloidal seed. Additionally the authors found outflow efficiencies $\langle \eta_j \rangle \geq 1$ if $|a| \geq 0.9$. The simulations we present in this work

Table 2. Peak, average value and standard deviation of the mass accretion rate at the event horizon and at $5r_g$, the normalised magnetic flux, and the energy outflow efficiency of the jet spine. Calculation interval $t = [5 - 10] \times 10^3 r_g/c$.

Res	$\dot{M}_{BH,max}$	$\langle \dot{M}_{BH} \rangle$	$\dot{M}_{5r_g,max}$	$\langle \dot{M}_{5r_g} \rangle$	$\varphi_{BH,max}$	$\langle \varphi_{BH} \rangle$	$\eta_{j,max}$	$\langle \eta_j \rangle$
R1	75.9	41.6 ± 10.5	47.1	20.1 ± 7.3	13.6	10.6 ± 1.5	2.30	1.12 ± 0.33
R2	59.2	36.6 ± 7.7	35.2	17.2 ± 5.8	13.0	10.9 ± 1.2	2.01	1.09 ± 0.29
R3	70.0	35.0 ± 7.8	46.2	17.0 ± 5.6	13.3	10.5 ± 1.3	2.87	1.15 ± 0.33
R4	65.0	39.8 ± 9.4	38.2	16.2 ± 5.9	14.3	11.3 ± 1.4	2.01	1.02 ± 0.28
R5	72.7	40.1 ± 9.5	38.9	15.7 ± 6.7	14.2	11.4 ± 1.8	2.64	0.99 ± 0.29

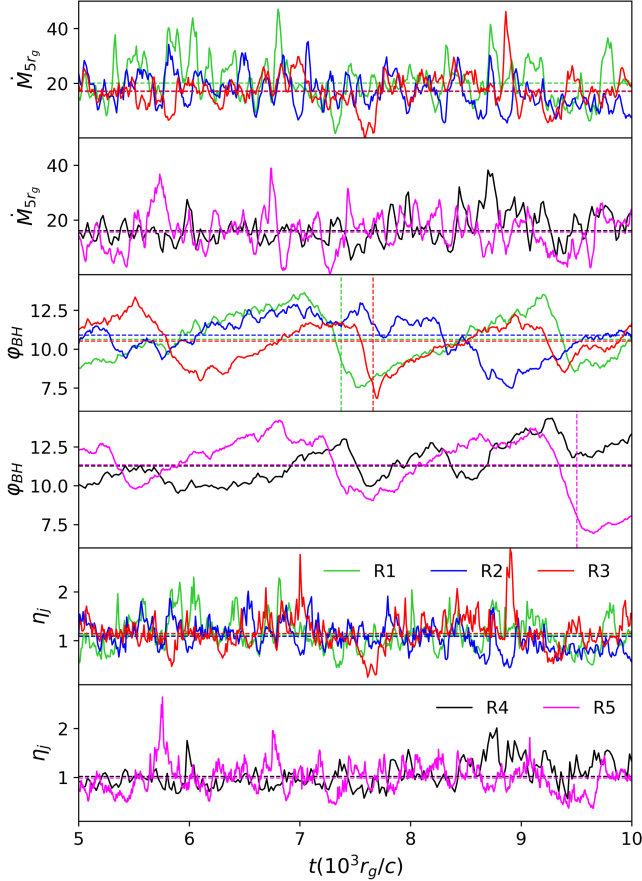


Figure 3. Mass accretion rate, normalised magnetic flux and jet outflow efficiency as a function of time in solid lines, together with the time averaged values in horizontal dashed lines. The magnetic flux saturates after $t = 5 \times 10^3 r_g/c$. The vertical dashed lines indicate the points where φ_{BH} approaches a local minimum (Fig. 1). The colour convention in all figures is resolution R1: green, R2: blue, R3: red, R4: black, and R5: purple.

are conducted with $a = 0.9375$, and we find outflow efficiencies $\langle \eta_j \rangle = [0.99 - 1.15] \pm 0.30$. We find that the outflow efficiency is converged within statistical uncertainty for the five resolutions considered (Table 2), where resolution R1 is similar to those used in Tchekhovskoy et al. (2011); McKinney et al. (2012). Additionally, we find that η_j fluctuates with time (Fig. 2) and has maximum values up to 2.87 (Table 2).

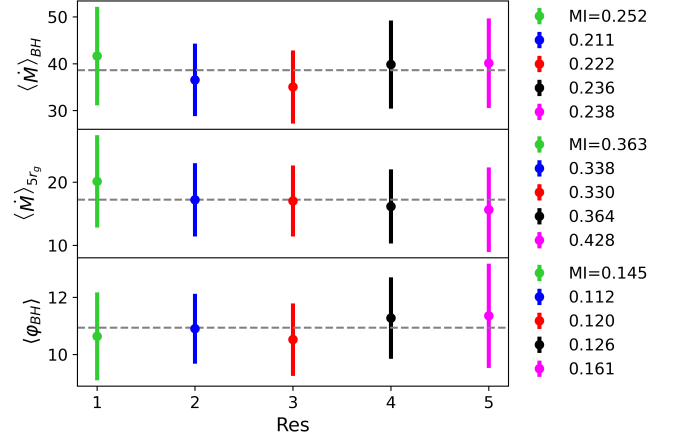


Figure 4. Resolution dependence of average values and standard deviations of mass accretion rate at the event horizon (top panel) and at $r = 5r_g$ (middle panel) and normalised magnetic flux (bottom panel). The horizontal grey line in each panel is the average value of all five resolutions, respectively. The modulation index is shown on the right. The error bars represent the standard deviations. Calculation interval $t = [5 - 10] \times 10^3 r_g/c$.

3.1.2 Flux eruptions

The variation in the amount of major flux eruptions observed across different resolutions, as depicted in Fig. 2 and 3, raises two key points: 1) Periodicity may not be directly linked to resolution, and 2) variations in periodicity suggest that it might not be inherently indicative of a periodic physical phenomenon. However, the statistics of these findings are limited by the relatively short duration of our high resolution simulations (see e.g. Narayan et al. 2012).

Fig. 5 displays the mid-plane density structures of the disks for all resolutions at different times. Low-density bubbles supported by magnetic pressure initially rise buoyantly away from the black hole and tend to orbit at a radius of $\approx 40r_g$. The sizes of these bubbles are relatively constant regardless of resolution. Smaller flux eruptions, such as shorter ones, tend to yield smaller bubbles, while larger flux eruptions typically lead to the formation of larger bubbles. Gravity naturally pulls inward, directing denser material towards the center. In this case, the lower density bubbles are prone to gravitational mixing instabilities such as RTI (Tchekhovskoy et al. 2011; Porth et al. 2021; Ripperda et al. 2022; Zhdarkin et al. 2023). At the lowest resolution R1, numerical diffusion causes the bubbles to mix. At higher resolution, finer structures are resolved because of mixing instabilities occurring at the surfaces of the bubbles.

There is a mixing of the low density bubbles with the higher density plasma in the accretion disk. This mixing causes mass to be advected inside the bubbles leading to a subsequent increase in the bubble density. At resolution R2, single plumes of high density plasma

develop, and these plumes often split a bubble into two separate bubbles. From resolution R3 and higher, increasingly more plumes develop simultaneously in a single bubble.

Additional work is needed to quantitatively determine the resolution dependence on the time evolution of the volume, magnetisation, temperature and energy contained within the bubbles (see e.g. Porth et al. 2021), the exact role of the mixing instabilities, how mixing impacts the polarisation signatures of magnetic flux eruptions in the radio band (e.g. Jia et al. 2023; Davelaar et al. 2023; Najafi-Ziyazi et al. 2024), or non-thermal particle acceleration (e.g. Zhdankin et al. 2023).

3.1.3 Viscosity Parameters

In this section, we study turbulence in the magnetised disk, which serves as a means to transfer angular momentum and energy. By making a decomposition of the velocity $\langle \vec{u} \rangle_{\rho[\theta, \phi]}^{\text{disk}} + \delta \vec{u}$ (disk average plus fluctuation) in the momentum conservation equation, a turbulent stress tensor is obtained. This tensor has two components: Reynolds and Maxwell stress tensors, which represent the statistical correlations of velocity and magnetic field components respectively. Angular momentum transport and extraction of available energy from the flow to fuel the turbulent fluctuations is provided by the turbulent stress tensor in the orbiting plasma (Balbus & Hawley 1998).

A viscosity parameter is often related to the strength of the radial and azimuthal turbulent speed correlations, $\delta u^r = u^r - \langle u^r \rangle_{\rho[\theta, \phi]}^{\text{disk}}$ and $\delta u^\phi = u^\phi - \langle u^\phi \rangle_{\rho[\theta, \phi]}^{\text{disk}}$, respectively. We recast the turbulent stresses in the classical alpha-models as follows (e.g. Shakura & Sunyaev 1973; Balbus & Hawley 1998; Liska et al. 2019; Chatterjee & Narayan 2022). The Reynolds viscosity is defined as:

$$\alpha_r \equiv \frac{\left\langle \left(\rho + u_g + p_g + b^2 \right) \delta u^r \sqrt{g_{rr}} \delta u^\phi \sqrt{g_{\phi\phi}} \right\rangle_{\rho[\theta, \phi]}^{\text{disk}}}{\langle \rho \rangle_{\rho[\theta, \phi]}^{\text{disk}}}, \quad (12)$$

and the Maxwell viscosity as:

$$\alpha_M \equiv - \frac{\langle b^r \sqrt{g_{rr}} b^\phi \sqrt{g_{\phi\phi}} \rangle_{\rho[\theta, \phi]}^{\text{disk}}}{\langle \rho \rangle_{\rho[\theta, \phi]}^{\text{disk}}}. \quad (13)$$

where, $p = b^2/2 + p_g$ is the total pressure. The time averaged viscosities in the disk are presented in bottom left panel of Fig. 6. We find that the Maxwell component dominates over the Reynolds component. The negative values of α_r indicate inward angular momentum transport and suggest convection-like behaviour (e.g. Begelman et al. 2022). The relatively low values of α_r indicate that the angular momentum transport due to turbulent convection is subdominant (e.g. Chatterjee & Narayan 2022). As demonstrated in previous works (e.g. Liska et al. 2019), the combination of both Reynolds and Maxwell viscosities is not sufficient to explain the total angular momentum transport, provided by the effective viscosity:

$$\alpha_{\text{eff}} \equiv - \frac{\langle v^r \sqrt{g_{rr}} v^\phi \sqrt{g_{\phi\phi}} \rangle_{\rho[\theta, \phi]}^{\text{disk}}}{\langle c_s^2 \rangle_{\rho[\theta, \phi]}^{\text{disk}}}, \quad (14)$$

where $v^r = u^r/u^t$ and $v^\phi = u^\phi/u^t$ are the physical radial and azimuthal velocity components, and the sound speed c_s is:

$$c_s \equiv \left| \frac{\gamma_{\text{ad}}(\gamma_{\text{ad}} - 1)u_g}{\rho + u_g + p_g} \right|^{1/2}. \quad (15)$$

The magnetorotational instability (MRI) is responsible for the generation of MHD turbulence that leads to enhanced outward angular momentum transport in accretion discs (Shakura & Sunyaev 1973; Balbus & Hawley 1998; Pessah et al. 2006). In this context, the Maxwell stress is associated to MRI. As seen in Fig. 6, for $r = [3 - 50] r_g$, there is a significant contribution of MRI to transport angular momentum, since the Maxwell viscosity is only a factor of ≈ 3 lower than the effective viscosity. For the very inner part of the accretion disk, $r < 3r_g$, α_{eff} keeps growing while α_M drops significantly. For MAD models, magnetic flux eruption-driven disk winds cause a strong vertical flow of angular momentum (Chatterjee & Narayan 2022) and jets can remove angular momentum close to the black hole (e.g. Tchekhovskoy et al. 2012; Narayan et al. 2022).

3.1.4 Magnetorotational Instability

The MRI quality factor components Q^i in the $i = [r, \theta, \phi]$ -direction are defined as the number of cells available for resolving the fastest-growing MRI mode wavelength:

$$Q^i \equiv \frac{2\pi r v_A^i}{\Delta x^i}, \quad (16)$$

where the size of the cell is $\Delta x^i \equiv dx^i \sqrt{g_{ii}}$. The Alfvén speed, which is the characteristic speed of transverse shear waves in a magnetized fluid (Balbus & Hawley 1998), is defined as:

$$v_A^i \equiv \left(\frac{|b^i b^i g_{ii}|}{\rho + u_g + p_g + b^2} \right)^{1/2}, \quad (17)$$

and the speed of the fluid is:

$$v \equiv \frac{\left(u^r u^r g_{rr} + u^\theta u^\theta g_{\theta\theta} + u^\phi u^\phi g_{\phi\phi} \right)^{1/2}}{u^t}. \quad (18)$$

The quality factors in all three directions are presented in the bottom panel of Fig. 6. For all simulations, the quality factors are large enough to sustain the MRI-driven turbulence. The only exception is the polar component Q^θ both near the event horizon ($r < 3r_g$) and further away in the disk ($40r_g \leq r \leq 100r_g$) for the lowest resolution R1. $Q^\theta < 10$ due to the coarse size of the cell and to the relatively lower Alfvén speed in the polar direction. However, this does not significantly affect the time-averaged accretion rate or normalised magnetic flux, as they consistently converge across all five resolutions.

Apart from the saturation of magnetic flux, another characteristic of the MAD state is the suppression of the MRI due to the strong magnetic fields close to the event horizon. Igumenshchev et al. (2003); Igumenshchev (2008) in pseudo-Newtonian MHD, and Tchekhovskoy et al. (2011); McKinney et al. (2012) via GRMHD simulations, demonstrated the suppression of MRI when poloidal magnetic flux saturates near the BH, forming a MAD. White et al. (2019) showed that the suppression of MRI is robust with resolution. From the general-relativistic dispersion relation connecting the Alfvén frequency (as seen by an observer at infinity) to oscillation frequency, Gammie (2004) proposed an instability criterion for the critical wavelength:

$$\lambda_{\text{crit}} \equiv 2\pi v_A^z \frac{r^{3/2} + a}{3^{1/2} (1 - 2r^{-1} + a^2 r^{-2})^{1/2}}. \quad (19)$$

The MRI is suppressed if the critical wavelength is bigger than the full height of the disk, $\langle \lambda_{\text{crit}} \rangle_{\rho[\theta, \phi]}^{\text{disk}} > H$ (White et al. 2019). The full height is defined geometrically as $H \equiv r \langle |\theta - \pi/2| \rangle_{\rho[\theta, \phi]}^{\text{disk}}$.

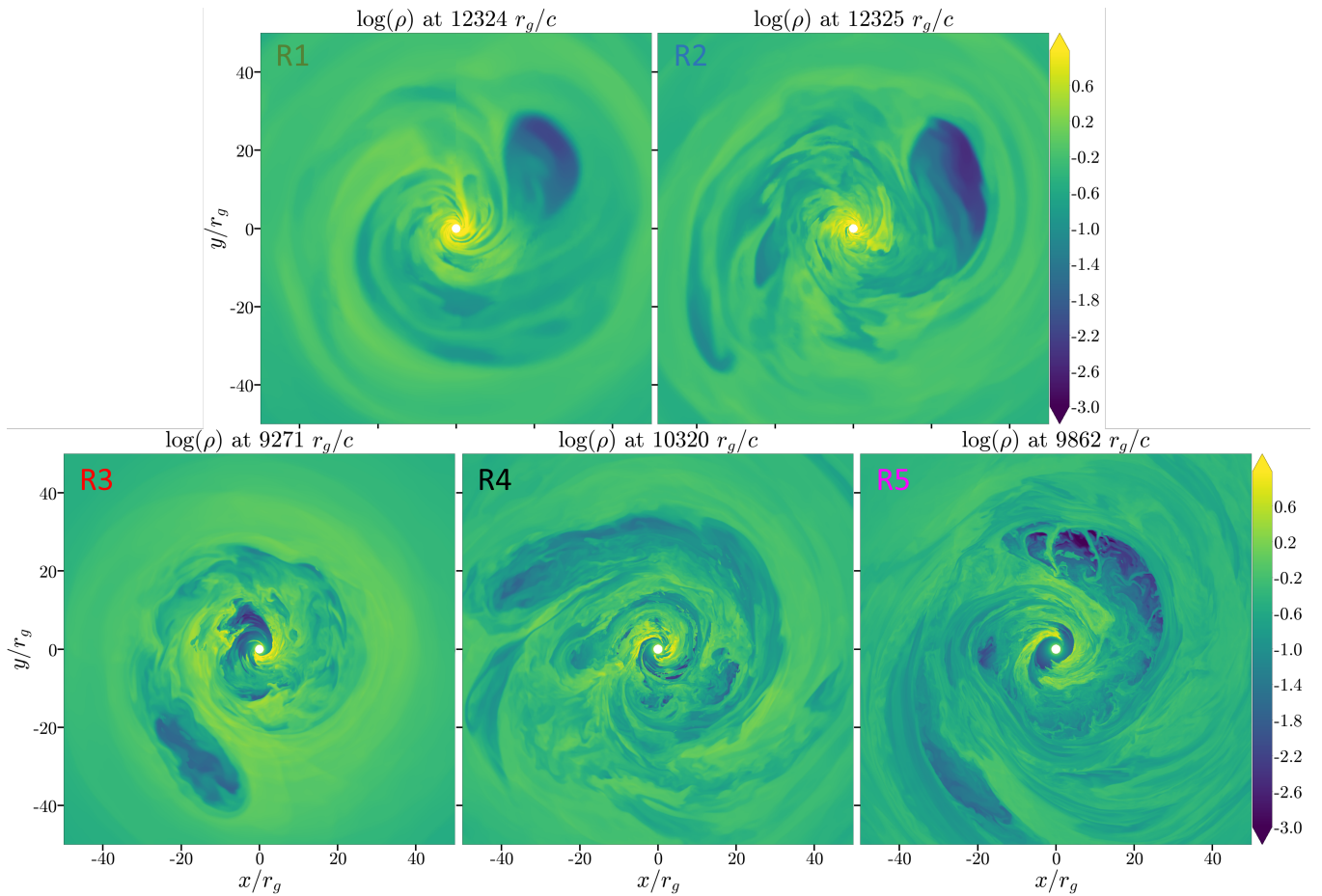


Figure 5. Equatorial 2D slices through $\theta = \pi/2$ of density ρ showing low density and high magnetisation flux tubes penetrating the accretion disk up to a radius of $\approx 40r_g$. From left to right: resolution R1 to R2 (top) and R3 to R5 (bottom).

As a consequence of the disk magnetic field strength increasing with resolution, the MRI is more suppressed according to the criterion $\langle \lambda_{crit} \rangle_{\rho[\theta, \phi]}^{\text{disk}} > H$. The degree of the suppression of MRI in GRMHD simulation depends on whether the simulation is performed in 2D or 3D, alongside the numerical resolution used (see e.g. White et al. 2019). In axisymmetric 2D simulations, the MRI turbulence decays after time intervals of $\sim 1000r_g/c$ (e.g. Hide & Palmer 1982; Balbus & Hawley 1991; Guan & Gammie 2008) and the most unstable axisymmetric linear mode of MRI is stabilised (e.g. McKinney et al. 2012; Begelman et al. 2022). Begelman et al. (2022) found that MRI is not completely suppressed in non-axisymmetric MAD flows, where the saturation of magnetic flux is driven by radial convective/interchange instabilities triggered by a dominant toroidal field. The MRI is a MHD instability originally introduced for axisymmetric, magnetized accretion disks (Balbus & Hawley 1998). Goedbloed & Keppens (2022) argue that axisymmetric MRIs represent only a finite amount of unstable modes and that turbulence, accretion and dynamo activity in 3D disks is governed by the excitation of nonaxisymmetric super-Alfvénic rotational instabilities (SARIs).

3.1.5 Plasmoids

During an eruption in MAD states, the expulsion of magnetic flux goes through the magnetic reconnection of field lines in a current

sheet in the equatorial plane. If this current sheet is sufficiently thin (see criteria for current sheet thickness δ below) such that plasmoid-mediated reconnection is resolved, then the current sheet can show signs of the tearing instability (Ripperda et al. 2020, 2022). Evidence of the plasmoid instability acting in the current sheet signifies that the rate at which magnetic energy is converted to heat, the reconnection rate, has converged to a value of $v_{\text{rec}} = 0.01v_A$ (Bhattacharjee et al. 2009; Uzdensky et al. 2010), where $v_A = \sqrt{\sigma/(\sigma+1)}c$ is the Alfvén speed. The plasmoid instability is typically triggered when the ratio between the alfvénic timescales and diffusion timescales, the Lundquist number $S \equiv v_A \omega / \eta \gtrsim 10^4$, where ω is the length of the current sheet (Bhattacharjee et al. 2009; Uzdensky et al. 2010). In this picture the thickness of the reconnection layer, δ , or rather its aspect ratio δ/ω , must match the asymptotic reconnection rate to minimally resolve the tearing instability, $v_{\text{rec}} = v_{\text{in}}/v_A = 0.01 = \delta/\omega$, where v_{in} is the inflow velocity into the layer, equal to the $\mathbf{E} \times \mathbf{B}/B^2$ -velocity in the direction perpendicular to the layer.

In ideal (GR)MHD, a current sheet, i.e., a magnetic null in the case of zero guide field as applicable to the equatorial current sheet in a MAD state (Ripperda et al. 2022), is only captured by a single cell (since it is governed by a numerical resistivity, see below). Therefore, for a current sheet that tears at $r = 2r_g$ (approximately at the ergosphere), one requires 1 cell per $\delta = 0.01r_g$ for a current sheet of length $\omega = 1r_g$. Comparing to the domain size (poloidal angle $\theta \in [0, \pi]$), this results in $2\pi r_g / 0.01r_g \gtrsim 600$ cells at $2r_g$,

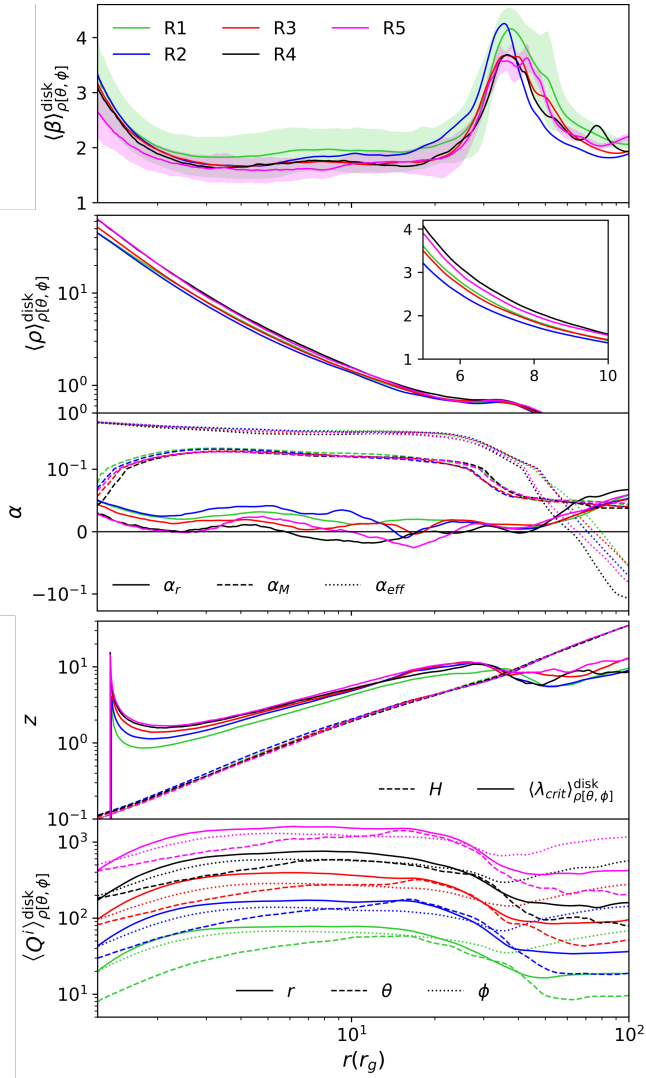


Figure 6. Time averaged, disk averaged profiles of variables as a function of radius. First panel: plasma beta $\beta = p_g/p_b$, gas-to-magnetic pressure ratio. Second panel: density. Third panel: viscosity parameters, Maxwell, Reynolds and Effective viscosity. Fourth panel: full height and critical wavelength. Fifth panel: quality factors. All the variables are averaged in time $t = [8 - 10] \times 10^3 r_g/c$. For plasma beta, shaded region depicts the range of variation within one standard deviation for R1 and R5. In flux eruption events, highly magnetised plasma from the jet spine penetrates the disk mid-plane ($r \lesssim 40r_g$) and propagates above and below the mid-plane ($40r_g \lesssim r \lesssim 100r_g$). As a consequence, the time averaged magnetic pressure (plasma beta) in the disk increases (decreases) with resolution.

implying that only simulations R4 and R5 have enough resolution in θ to minimally resolve the tearing instability near the horizon for current sheets of length $\omega \geq 1r_g$, as indicated by our results below.

In ideal GRMHD simulations, such as those conducted here, reconnection is mediated via numerical resistivity η_{num} instead of an explicit resistivity η (Ripperda et al. 2019). We can determine whether our simulations are computed with sufficient numerical accuracy in order to resolve plasmoid-mediated reconnection, and thus form plasmoids by calculating the numerical Lundquist number $S \equiv v_A \omega / \eta_{\text{num}}$, where $\eta_{\text{num}} = \hat{C} \Delta x$ and the coefficient \hat{C} depends on the accuracy and order of the reconstruction scheme (Zhang et al. 2003). In the plasmoid instability regime, the rate of magnetic flux

decay on the horizon converges to $\varphi_{\text{BH}} \propto e^{-t/500}$ (Bransgrove et al. 2021; Ripperda et al. 2022). In simulations R4 and R5 we observe plasmoids in current sheets of length $\omega \sim 10r_g$ close to the event horizon, indicating that resolutions of a minimum of $2240 \times 1056 \times 1024$ are required to resolve the plasmoid instability, see Fig. 4 and Appendix C of Ripperda et al. (2022). Based on these results, the constant $\hat{C} \approx 0.03$ is obtained by setting $10^4 = 10/\eta_{\text{num,R4}}$, where $\eta_{\text{num,R4}}$ is the numerical resistivity at $10r_g$ for R4. The Alfvén speed $v_A = \sqrt{25/26}c \approx c = 1$ for the reconnecting plasma because the reconnection is fed by the plasma in the jet at $\sigma_{\text{max}} = 25$. Due to the use of a spherical grid, it is harder to resolve plasmoid-mediated reconnection at larger radii and in smaller current sheets, due to the reduction in resolution at larger radii.

3.1.6 Disk profiles

The time averaged profiles of the disk plasma beta (ratio of gas-to-magnetic pressure $\beta = p_g/p_b$), density, viscosity parameters (Maxwell, Reynolds and effective viscosity), full height, critical wavelength and quality factors are presented in Fig. 6. All variables presented in Fig. 6 are averaged between 8 to $10 \times 10^3 r_g/c$.

2D slices through azimuthal angle $\phi = 0$ of plasma beta β are shown in Fig. 7. We find that the jet spine gets more magnetised with increasing resolution as demonstrated in Section 3.2 (Fig. 8). During flux eruption events, highly magnetized flux tubes originating from the jet spine penetrate the disk and propagate until $r \lesssim 40r_g$. The pressure maximum of the initialised Fishbone-Moncrief torus is located at $r = 41r_g$ —at around this radius, the flux tubes split into two and are ejected as outflows above and below the disk mid-plane. These ejections increase the time-averaged disk magnetic pressure, and consequently reduce the plasma beta in the disk, as observed in Fig. 6. Plasma beta in the disk for $r \gtrsim 3r_g$ is convergent for resolutions R3 and higher. For resolution R5, plasma beta for $r \lesssim 3r_g$ is slightly lower than the rest of simulations. Very close to the BH $r \lesssim 3r_g$, the Maxwell viscosity drops significantly for all resolutions. In this inner part of the accretion disk, the vertical magnetic pressure is responsible for launching winds that transport angular momentum outwards (e.g. Chatterjee & Narayan 2022).

3.2 Jet Properties

The averaged profile of a jet variable does not involve any density or magnetisation weight. For the jet spine:

$$\langle X \rangle_{[\theta, \phi]}^{\text{spine}} = \frac{\iint X(\sigma > 1) \sqrt{-g} d\theta d\phi}{\iint (\sigma > 1) \sqrt{-g} d\theta d\phi}, \quad (20)$$

and for the jet sheath:

$$\langle X \rangle_{[\theta, \phi]}^{\text{sheath}} = \frac{\iint_{|\pi - \theta| \leq \pi/6} X(\sigma < 1) (Be > 1.02) \sqrt{-g} d\theta d\phi}{\iint_{|\pi - \theta| \leq \pi/6} (\sigma < 1) (Be > 1.02) \sqrt{-g} d\theta d\phi}. \quad (21)$$

We follow the methodology used in Chatterjee et al. (2019) to investigate the instabilities occurring in the jet sheath-spine interface. Decomposing the stress-energy tensor $T^r_t \equiv (T_H)^r_t + (T_M)^r_t$ (Equation 4), with the hydro component:

$$(T_H)^r_t \equiv (\rho + u_g + p_g) u^r u_t, \quad (22)$$

and magnetic component:

$$(T_M)^r_t \equiv b^2 u^r u_t - b^r b_t, \quad (23)$$

We define the total specific energy, measuring the maximum

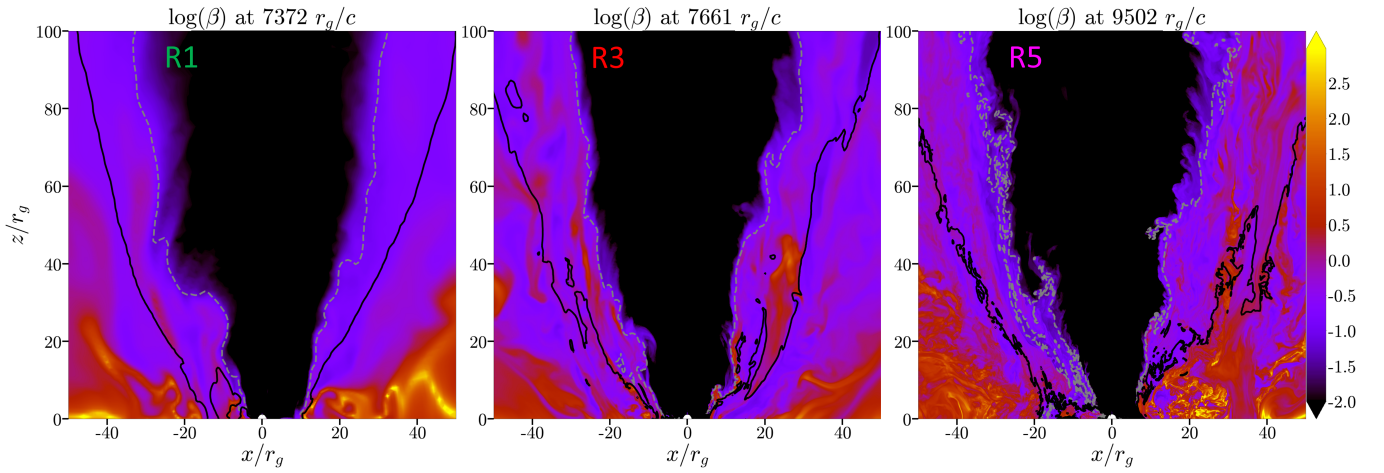


Figure 7. Meridian 2D slices through $\phi = 0$ for plasma beta $\beta = p_g/p_b$. From left to right: resolution R1, R3 and R5. The grey dashed and black lines correspond to surfaces where $\sigma = 1$ and $Be = 1.02$, respectively. We partially cover the spine with a zero screen activated for $\sigma > 3$, allowing visibility of plasma within the range of $1 < \sigma < 3$. As resolution increases, the polar axis features a smaller volume and therefore there is less dissipation of magnetic energy along the pole. In flux eruption events, highly magnetised plasma from the jet spine penetrates the disk, causing the time averaged plasma beta in the disk to decrease with resolution.

Lorentz factor if all forms of energy are converted into kinetic energy,

$$\mu \equiv \frac{\langle T^r_t \rangle_{[\theta, \phi]}^{\text{spine}}}{\langle -\rho u^r \rangle_{[\theta, \phi]}^{\text{spine}}}, \quad (24)$$

the magnetisation, as a measure of conversion efficiency of kinetic to magnetic energy,

$$\hat{\sigma} \equiv \frac{\langle (T_M)^r_t \rangle_{[\theta, \phi]}^{\text{spine}}}{\langle (T_H)^r_t \rangle_{[\theta, \phi]}^{\text{spine}}}, \quad (25)$$

the specific enthalpy,

$$h \equiv \frac{\langle T^r_t (u_g + p_g) / \rho \rangle_{[\theta, \phi]}^{\text{spine}}}{\langle T^r_t \rangle_{[\theta, \phi]}^{\text{spine}}}, \quad (26)$$

and the Lorentz factor,

$$\gamma \equiv \frac{\langle T^r_t u^t \sqrt{-1/g^{tt}} \rangle_{[\theta, \phi]}^{\text{spine}}}{\langle T^r_t \rangle_{[\theta, \phi]}^{\text{spine}}}. \quad (27)$$

The energy equation can be obtained by combining the four previously defined variables:

$$\mu = \gamma (\hat{\sigma} + 1) (h + 1). \quad (28)$$

3.2.1 Jet spine

The top panel of Fig. 8 shows the total specific energy, magnetisation, enthalpy, Lorentz factor and half opening angle of the upper jet spine (Equation 20), each of which are averaged over the time interval $t = [8 - 10] \times 10^3 r_g/c$. We find that the Lorentz factor is nearly the same for all resolutions presented, and increases from approximately 2 to 7 with radius $20 - 10^3 r_g$. The total specific energy is convergent and nearly constant with radius. However, the magnetisation and enthalpy are convergent only for resolutions R4 and R5 and are not physically trustworthy.

Since numerical dissipation is proportional to the cell size, as the resolution increases the cells get smaller. Consequently, cells near the polar axis have a smaller volume which results in less dissipation of magnetic energy and heating along the pole. As a result the jet spine gets more magnetised, $\hat{\sigma}$ drops notably slower with radius, and the internal gas energy and pressure decrease with resolution as shown in Fig. 1. Properties such as magnetisation and enthalpy in the jet become unreliable if number of cells per half opening angle drops below 10 (see bottom panel of Fig. 8). Additionally, the polar axis introduces considerable uncertainty into thermodynamics—while the transmissive boundary conditions used at the poles effectively capture the flow of energy, they artificially change the conversion of one energy source into another.

The half opening angle of the jet spine is slightly higher for R4 and R5, especially close to the base of the jet. The standard deviation of the half opening angle decreases with radius. Close to the black hole, $r < 50 r_g$, we see high fluctuations in the width of the jet spine and sheath due to the magnetic flux eruptions in the MAD states.

3.2.2 Jet sheath

The top panel of Fig. 9 shows the total specific energy, magnetisation, enthalpy, Lorentz factor, and half opening angle of the jet sheath, all averaged over the time interval $t = [8 - 10] \times 10^3 r_g/c$. In general, all these variables in the sheath are lower than the corresponding values in the spine, except the enthalpy for $r \lesssim 60 r_g$ where $h_{\text{sheath}} > h_{\text{spine}}$ for R4 and R5. The enthalpy for R1 has an inflection point around $100 r_g$, where h starts to increase due to enhanced numerical dissipation caused by a lack of resolution in the polar direction.

When a flux eruption occurs, $\hat{\sigma}$ drops locally at the base of the jet generating a wave that propagates outwards. This wave is accompanied by a simultaneous increase of enthalpy, creating a thermal pressure gradient that slows down the jet outflow (see Fig. 10). However, the Lorentz factor of the jet γ only decreases a few percent for all resolutions. In contrast, Chatterjee et al. (2019) found a significant reduction of γ at $r \approx 10^3 r_g$ when pinch instabilities cause magnetic dissipation, that raise the jet specific enthalpy to order unity. The fact that we do not see such a significant reduction of γ in our simula-

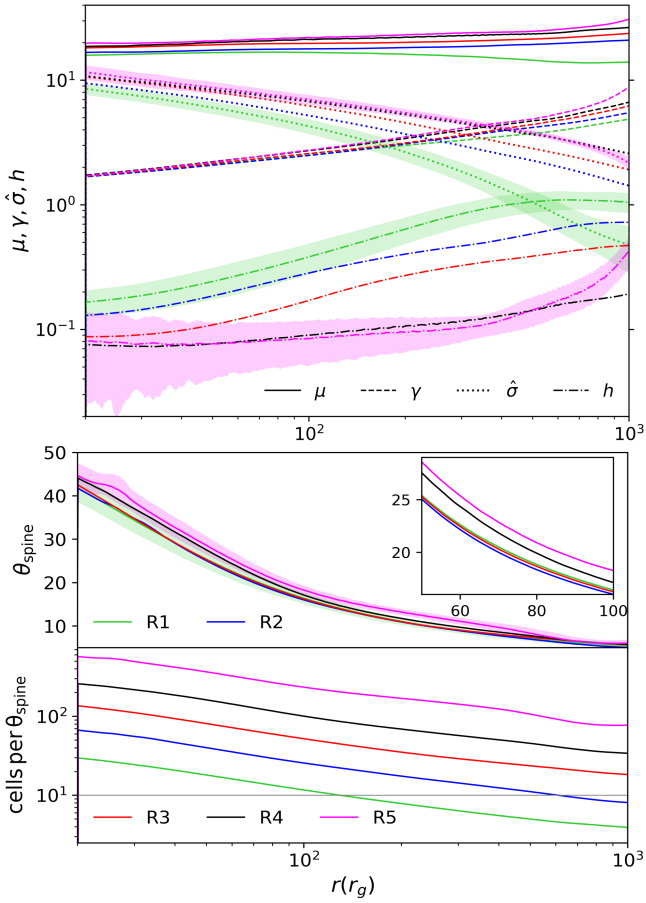


Figure 8. Jet spine ($\sigma > 1$) properties as a function of r , averaged in time $t = [8 - 10] \times 10^3 r_g / c$. Total specific energy, Lorentz factor, magnetisation and enthalpy (top panel). Half opening angle (middle panel) and cells per half opening angle (bottom panel). Shaded regions depict the range of variation within one standard deviation for R1 and R5. $\hat{\sigma}$ and h are not physically trustworthy. Additionally, the jet spine is wider for R4 and R5.

tions is a consequence of the much smaller disc that collimates the jet out to approximately $500 r_g$. For $r > 500 r_g$, the diminishing confining pressure exerted by the disk wind triggers a lateral expansion of the jet, effectively suppressing pinch instabilities (see, e.g., Porth & Komissarov 2015). This expansion of the jet leads to acceleration and increase of γ .

Mixing instabilities due to shearing motions across the interface between the jet and the accretion disk can potentially cause the dissipation of magnetic energy into heat. Resolving these mixing instabilities is crucial for comprehending the energetic dynamics of jets at large radii, as mixing will lead to mass loading of the jet. Close to BH, the jet is primarily loaded by material from density floors. We see wave-like features in the jet sheath, which become more prominent (less diffusive) at higher resolutions. These wave-like features may induce mixing between jet, sheath and disk (see Fig. 1 and 7). In addition to affecting the degree of mass loading in the jet, the wave-like features in the jet sheath may also affect the magnetic field in the proximity of the jet sheath: Davelaar et al. (2023) found that waves propagating along the jet-wind shear layer alter the orientation of the magnetic field lines.

For $r \lesssim 100 r_g$, the half opening angle of the sheath features strong fluctuations and on average the sheath is thinner at resolutions R3,

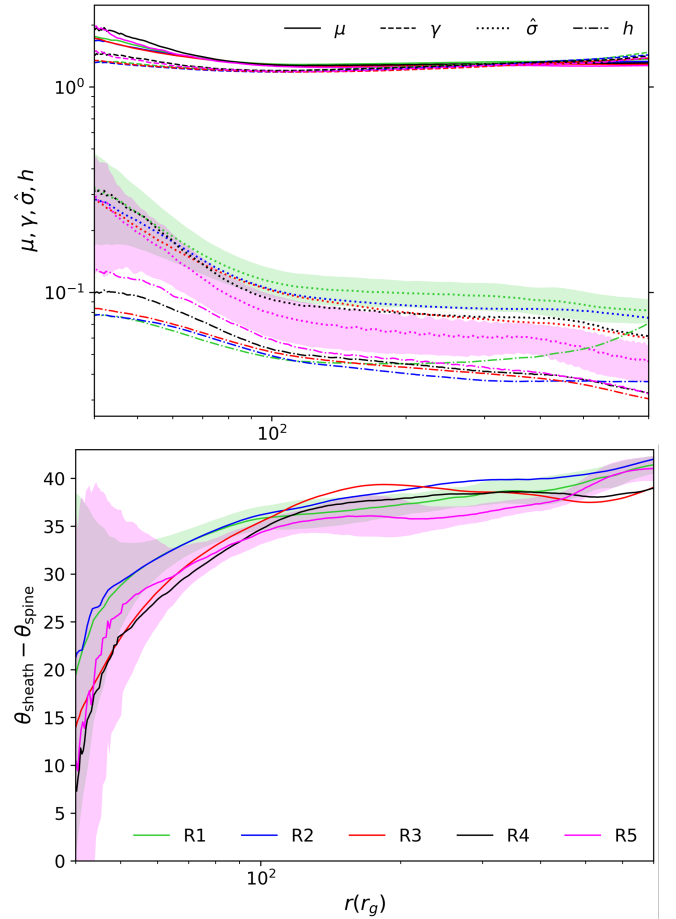


Figure 9. Jet sheath properties as a function of r , averaged in time $t = [8 - 10] \times 10^3 r_g / c$. Total specific energy, Lorentz factor, magnetisation and enthalpy (top panel). Half opening angle of the jet sheath measured from the jet spine (bottom panel). Shaded regions depict the range of variation within one standard deviation for R1 and R5. Mixing instabilities occurring in the jet sheath-spine interface cause a reduction of magnetisation and increase of enthalpy with resolution.

R4 and R5 (see bottom panel of Fig. 9). Between 100 and $\approx 500 r_g$, the sheath is thinner at resolution R5. This slimming of the jet sheath can result in an increase of enthalpy and reduction of magnetisation in the sheath, while keeping an approximately constant total specific energy for all resolutions: These results have a direct impact on the temperature, as described in Section 3.2.3.

3.2.3 Proton temperature

The proton temperature in the jet sheath and disk is presented in Fig. 11. The protons in the disk are near virial temperature $\propto r^{-1.3}$, and T_p in the disk is converged for all resolutions we consider. On the other hand, T_p in the sheath is found to increase with increasing resolution. Processes causing a mixing of the colder jet sheath with the hotter jet spine can include: (1) mixing instabilities due to shearing motion across the interface between the jet sheath and funnel, (2) waves generated at the jet base in MAD states that propagate along the jets and, (3) wobbling of the jet itself (see e.g. Wong et al. 2021; Davelaar et al. 2023). In addition, the increase we see in the magnetisation of the jet spine as the resolution is increased

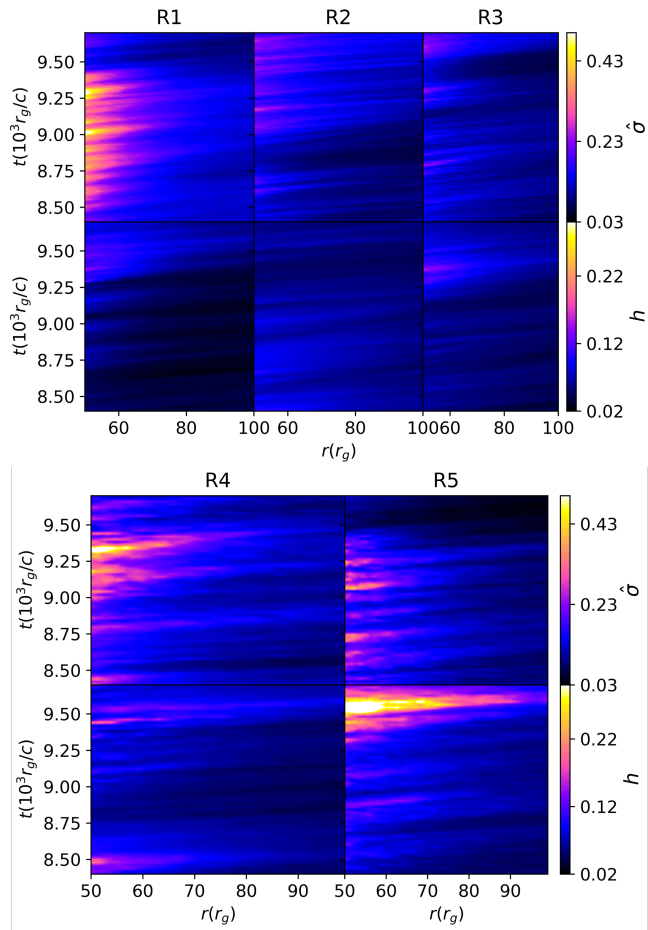


Figure 10. Space-time diagrams of magnetisation (top panels) and enthalpy (bottom panels) of the jet sheath. From left to right: resolution R1 to R5. A localised decrease in $\hat{\sigma}$ is accompanied by a simultaneous rise in enthalpy, generating a wave that propagates outwards.

also impacts T_p in the sheath. Highly magnetised plasma from the jet spine supplies matter to the current sheet, with $T_p \propto \sigma_{spine}$, and the reconnection exhaust deposits this hot plasma in the jet sheath up to at least $20r_g$ for resolutions R4 and R5 (Ripperda et al. 2022). For $r < 100r_g$, the sheath is thinner at higher resolution (see Fig. 9), the amount of dissipation/heating gets distributed across a smaller volume of plasma, leading to higher maximum temperature. The jet sheath (proton) temperatures are non fully convergent with resolution. Despite this, T_p varies by less than a factor of ~ 2 between the lowest and highest resolutions.

The proton temperature in the jet sheath follows a shallower profile, $\propto r^{-0.3}$, than in the disk $\propto r^{-1.3}$. The jet is well collimated by the large disk when the numerical resolution is adequate for capturing the jet at large radii away from the black hole. The proton temperature profile in the jet sheath is different for the lowest resolution level R1. In this case, T_p remains nearly constant for radii between 100 and $500r_g$, and then follows a power law of $\propto r^{-0.3}$ at larger radii. This discrepancy arises from a lack of resolution in the polar direction at $r > 100r_g$ along the jet axis for R1 compared to the other resolutions we present.

Our simulations show that the adiabatic decompression of the jet sheath begins at around $500r_g$, where the temperature gradient is much steeper than $r^{-0.3}$ (Fig. 11). It is worth mentioning that

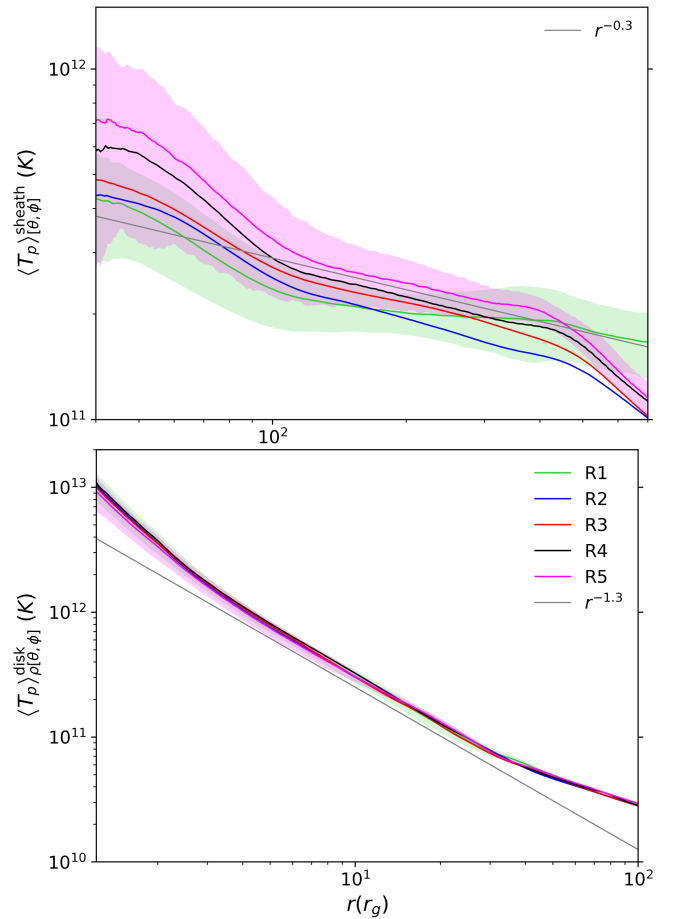


Figure 11. Proton temperature in the jet sheath (top panel) and in the disk (bottom panel). All averaged in $t = [8 - 10] \times 10^3 r_g/c$. Shaded regions depict the range of variation within one standard deviation for R1 and R5.

the change in steepness of the temperature gradient depends on the size of the initial torus, and it is unknown whether this adiabatic decompression happens in real systems. For instance, observations utilising the Very Large Array (VLA) have revealed a parabolic collimation profile in the M87* jet extending up to $10^5 r_g$ (Asada & Nakamura 2012; Hada et al. 2013; Mertens et al. 2016; Kim et al. 2018; Nakamura et al. 2018).

4 CONCLUSIONS

GRMHD codes face significant numerical challenges when used to perform simulations in the MAD regime. The higher magnetic flux characteristic of the MAD regime leads to new dynamics, including interchange-type accretion modes, suppression of MRI and flux eruptions governed by plasmoid dominated magnetic reconnection. The occurrence and dynamics of these phenomena may be affected by the numerical resolution of GRMHD MAD simulations. Recently, White et al. (2019) conducted a resolution study of MAD accretion flows, with simulations reaching a maximum effective resolution of $512 \times 256 \times 512$. They showed that the general large-scale structure of the accretion flow is robust with resolution, for the resolutions they considered. However, they found that the spatial structure and Lorentz factor of the jet, small-scale features of the turbulence and variabil-

ity of modelled synchrotron emission were not fully converged with resolution.

We have conducted a study of MAD states and jets across a wider range of resolutions than has been previously explored, up to resolution of $5375 \times 2304 \times 2304$ in a logarithmic spherical-polar grid, using existing simulations in Ripperda et al. (2022). Such extreme resolution is needed to achieve convergence in the reconnection rate in the plasmoid-dominated regime in GRMHD, which is important for the timescale of variability. We divided the system in three components: the jet spine (relativistic and strongly magnetised outflow), the jet sheath (mildly relativistic outflow) and the disk. Below, we elucidate how our findings might influence ongoing studies within the black hole accretion community.

We find that the time-averaged disk properties are consistent for all resolutions with only small differences in flux variability, plasma beta and inferred viscosity parameters close to the BH. For resolution $2240 \times 1056 \times 1024$ and higher, we find that the time-averaged Reynolds viscosity, attributed to turbulent convection, indicates inward angular momentum transport around $10r_g$. Higher resolutions resolve finer structures when mixing instabilities occur at the surfaces of flux tubes during flux eruptions (see Fig. 5). This mixing may function as mechanism for energy dissipation, non-thermal particle acceleration and flare generation across various wavelengths.

For the jet spine, the total specific energy and Lorentz factor is nearly the same for all resolutions we consider. We find that the magnetisation and enthalpy are convergent for resolution $2240 \times 1056 \times 1024$ and higher. However, these four jet spine properties do depend on, and are governed by, the chosen magnetisation ceiling in the code setup. For this reason, we recommend caution in drawing conclusions based on jet dynamics in general, as the jet spine is dominated by numerical floors and the magnetisation and enthalpy are not physically reliable.

We find that the jet-disk interface, the "sheath" is the most sensitive region to resolution. There are large fluctuations in the width of the jet sheath due to magnetic flux eruptions for $r \lesssim 50r_g$, more prominent at higher resolutions. These fluctuations directly influence the variability of properties within the jet sheath, notably the temperature and magnetisation. At higher resolutions, we see more resolved wave-like features in the jet sheath, that may induce mixing between the sheath and plasma within $1 \lesssim \sigma \lesssim 3$ (see Fig. 1 and 7). Mixing processes may include (1) shearing motion across the interface between the jet sheath and spine, (2) propagation of waves generated at the jet base, and (3) wobbling of the jet itself. Additionally for resolution $2240 \times 1056 \times 1024$ and $5376 \times 2304 \times 2304$, highly magnetised plasma from the jet spine supplies matter to the current sheets, and the reconnection exhaust deposits this hot plasma into the jet sheath (Ripperda et al. 2022). At higher resolutions, we find that the jet sheath gets thinner, resulting in increased temperature, reduced magnetisation, and greater variability of T_p , $\hat{\sigma}$ and opening angle, while keeping an approximately constant total specific energy for all resolutions. These differences could affect the predicted multiwavelength spectra coming from the jet sheath, relevant to e.g. the EHT collaboration and VLBI imaging of large-scale jets. In the next paper on jet images, we will analyse whether a hotter, thinner jet sheath could result in increased limb-brightening in the observed images (e.g. Kim et al. 2018; Janssen et al. 2021) or potentially lead to filamentary structures observed in jets (Fuentes et al. 2023).

Capturing plasma mixing in flux tubes and along the jet-disk interface is essential for improved comparisons between observations and simulations. The presence of mixing instabilities could significantly influence the dissipation of energy, that could result in distinct multiwavelength emission from high-resolution simulations (e.g. Sironi

et al. 2021; Zhdankin et al. 2023). In forthcoming research we will investigate the influence of mixing instabilities on radiative emission in both total intensity and polarisation. We will focus on analysing non-thermal electron distribution functions on the dissipative regions. We will aim to simulate three-dimensional systems capable of accurately capturing jets extending up to $10^5 r_g$ or more. This research is relevant to studies of AGN, such as M87*. By doing so, we aspire to deepen our comprehension of the fundamental horizon-scale physical processes and their implications for the dynamics and emission properties of larger-scale jets.

ACKNOWLEDGEMENTS

We gratefully recognise Sasha Tchekhovskoy and Doosoo Yoon for insightful discussions. L.S. and S.M. were supported by a Dutch Research Council (NWO) VICI award, grant No. 639.043.513 and by a European Research Council (ERC) Synergy Grant "BlackHolistic" grant No. 101071643. In addition, L.S. was supported by the Colfuturo Scholarship. G.M. was supported by a Canadian Institute of Theoretical Astrophysics (CITA) postdoctoral fellowship and by a Netherlands Research School for Astronomy (NOVA), Virtual Institute of Accretion (VIA) postdoctoral fellowship. K.C. was supported in part by grants from the Gordon and Betty Moore Foundation and the John Templeton Foundation to the Black Hole Initiative at Harvard University, and by NSF award OISE-1743747. O.P. acknowledges funding from VIA within NOVA. ML was supported by the John Harvard, ITC and NASA Hubble Fellowship Program fellowships. B.R. is supported by the Natural Sciences & Engineering Research Council of Canada (NSERC) and by a grant from the Simons Foundation (MP-SCMPS-00001470). Research at the Flatiron Institute is supported by the Simons Foundation.

This research was enabled by support provided by grant no. NSF PHY-1125915 along with a INCITE program award PHY129, using resources from the Oak Ridge Leadership Computing Facility, Summit, which is a US Department of Energy office of Science User Facility supported under contract DE-AC05-00OR22725, as well as Calcul Quebec (<http://www.calculquebec.ca>) and Compute Canada (<http://www.computeCanada.ca>). The computational resources and services used in this work were partially provided by facilities supported by the Scientific Computing Core at the Flatiron Institute, a division of the Simons Foundation; and by the VSC (Flemish Supercomputer Center), funded by the Research Foundation Flanders (FWO) and the Flemish Government – department EWI. This research is part of the Frontera (Stanzione et al. 2020) computing project at the Texas Advanced Computing Center (LRAC-AST20008). Frontera is made possible by National Science Foundation award OAC-1818253. This work used the Dutch national e-infrastructure with the support of the SURF Cooperative using grant no. EINF-3036 and EINF-5383, which is (partly) financed by the Dutch Research Council (NWO), for post-processing of simulation data.

DATA AVAILABILITY

The simulation post-processed data used to plot the images in this work are available in Zenodo at <http://doi.org/10.5281/zenodo.10996780>

REFERENCES

- Acciari V. A., et al., 2010, *ApJ*, **716**, 819
- Aharonian F., et al., 2006, *Science*, **314**, 1424
- Akiyama K., et al., 2023, *ApJ*, **957**, L20
- Aliu E., et al., 2012, *ApJ*, **746**, 141
- Anninos P., Fragile P. C., Salmonson J. D., 2005, *ApJ*, **635**, 723
- Asada K., Nakamura M., 2012, *ApJ*, **745**, L28
- Baganoff F. K., et al., 2001, *Nature*, **413**, 45
- Balbus S. A., Hawley J. F., 1991, *Astrophysical Journal*, **376**, 214
- Balbus S. A., Hawley J. F., 1998, *Reviews of Modern Physics*, **70**, 1
- Begelman M. C., Scepi N., Dexter J., 2022, *MNRAS*, **511**, 2040
- Bhattacharjee A., Huang Y.-M., Yang H., Rogers B., 2009, *Physics of Plasmas*, **16**, 112102
- Bisnovatyi-Kogan G. S., Ruzmaikin A. A., 1974, *Ap&SS*, **28**, 45
- Blanch O., 2021, *The Astronomer's Telegram*, 14483, 1
- Blandford R. D., Znajek R. L., 1977, *Monthly Notices of the Royal Astronomical Society*, **179**, 433
- Bransgrove A., Ripperda B., Philippov A., 2021, *Phys. Rev. Lett.*, **127**, 055101
- Chatterjee K., Narayan R., 2022, *ApJ*, **941**, 30
- Chatterjee K., Liska M., Tchekhovskoy A., Markoff S. B., 2019, *Monthly Notices of the Royal Astronomical Society*, **490**, 2200
- Colella P., Woodward P. R., 1984, *JCoPh*, **54**, 174
- Davelaar J., Mościbrodzka M., Bronzwaer T., Falcke H., 2018, *Astronomy & Astrophysics*, **612**, A34
- Davelaar J., et al., 2023, *ApJ*, **959**, L3
- Del Zanna L., Zanotti O., Bucciantini N., Londrillo P., 2007, *A&A*, **473**, 11
- Dexter J., et al., 2020, *MNRAS*, **497**, 4999
- EHT MWL Science Working Group Algaba J. C., Anzarski J., Asada K., Baloković M., Chandra S., et al. 2021, *ApJ*, **911**, L11
- Eckart A., et al., 2004, *A&A*, **427**, 1
- Etienne Z. B., Paschalidis V., Haas R., Mösta P., Shapiro S. L., 2015, *Classical and Quantum Gravity*, **32**, 175009
- Event Horizon Telescope Collaboration Akiyama K., Alberdi A., Alef W., Asada K., et al. 2019a, *ApJ*, **875**, L1
- Event Horizon Telescope Collaboration Akiyama K., Alberdi A., Alef W., Asada K., et al. 2019b, *ApJ*, **875**, L5
- Event Horizon Telescope Collaboration Akiyama K., Algaba J. C., Alberdi A., Alef W., et al. 2021, *ApJ*, **910**, L13
- Event Horizon Telescope Collaboration Akiyama K., Alberdi A., Alef W., Algaba J. C., et al. 2022a, *ApJ*, **930**, L12
- Event Horizon Telescope Collaboration Akiyama K., Alberdi A., Alef W., Algaba J. C., et al. 2022b, *ApJ*, **930**, L13
- Event Horizon Telescope Collaboration Akiyama K., Alberdi A., Alef W., Algaba J. C., et al. 2022c, *ApJ*, **930**, L16
- Fabian A., 2012, *Annual Review of Astronomy and Astrophysics*, **50**, 455
- Fishbone L. G., Moncrief V., 1976, *The Astrophysical Journal*, **207**, 962
- Fuentes A., et al., 2023, *Nature Astronomy*, **7**, 1359
- GRAVITY Collaboration et al., 2018, *A&A*, **618**, L10
- Gammie C. F., 2004, *The Astrophysical Journal*, **614**
- Gammie C. F., McKinney J. C., Tóth G., 2003, *ApJ*, **589**, 444
- Gardiner T. A., Stone J. M., 2005, *Journal of Computational Physics*, **205**, 509
- Goedbloed H., Keppens R., 2022, *ApJS*, **259**, 65
- Gravity Collaboration Abuter R., et al., 2021, *Astronomy and Astrophysics*, **A&A**, **654**, A22
- Grete P., Glines F. W., O'Shea B. W., 2021, *IEEE Transactions on Parallel and Distributed Systems*, **32**, 85
- Guan X., Gammie C. F., 2008, *ApJS*, **174**, 145
- Hada K., et al., 2013, *ApJ*, **775**, 70
- Hakobyan H., Ripperda B., Philippov A. A., 2023, *ApJ*, **943**, L29
- Hide R., Palmer T., 1982, *Geophysical & Astrophysical Fluid Dynamics*, **19**, 301
- Igumenshchev I. V., 2008, *ApJ*, **677**, 317
- Igumenshchev I. V., Narayan R., Abramowicz M. A., 2003, *ApJ*, **592**, 1042
- Janssen M., et al., 2021, *Nature Astronomy*, **5**, 1017
- Jia H., Ripperda B., Quataert E., White C. J., Chatterjee K., Philippov A., Liska M., 2023, *MNRAS*, **526**, 2924
- Kim J. Y., et al., 2018, *A&A*, **616**, A188
- Liska M., Tchekhovskoy A., Ingram A., van der Klis M., 2019, *MNRAS*, **487**, 550
- Liska M., Tchekhovskoy A., Quataert E., 2020, *MNRAS*, **494**, 3656
- Liska M. T. P., et al., 2022, *ApJS*, **263**, 26
- Liska M. T. P., Kaaz N., Chatterjee K., Emami R., Musoke G., 2024, *ApJ*, **966**, 47
- McKinney J. C., Tchekhovskoy A., Blandford R. D., 2012, *MNRAS*, **423**, 3083
- Mertens F., Lobanov A. P., Walker R. C., Hardee P. E., 2016, *A&A*, **595**, A54
- Mościbrodzka M., Falcke H., 2013, *Astronomy & Astrophysics*, **559**, L3
- Najafi-Ziyazi M., Davelaar J., Mizuno Y., Porth O., 2024, *MNRAS*, **531**, 3961
- Nakamura M., et al., 2018, *ApJ*, **868**, 146
- Narayan R., Igumenshchev I. V., Abramowicz M. A., 2003, *PASJ*, **55**, L69
- Narayan R., Sadowski A., Penna R. F., Kulkarni A. K., 2012, *Monthly Notices of the Royal Astronomical Society*, **426**, 3241
- Narayan R., Chael A., Chatterjee K., Ricarte A., Curd B., 2022, *MNRAS*, **511**, 3795
- Neilsen J., et al., 2015, *The Astrophysical Journal*, **799**, 199
- Noble S. C., Gammie C. F., McKinney J. C., Zanna L. D., 2006, *The Astrophysical Journal*, **641**, 626
- Pessah M. E., Chan C.-K., Psaltis D., 2006, *MNRAS*, **372**, 183
- Porth O., Komissarov S. S., 2015, *MNRAS*, **452**, 1089
- Porth O., Olivares H., Mizuno Y., Younsi Z., Rezzolla L., Mościbrodzka M., Falcke H., Kramer M., 2017, *Computational Astrophysics and Cosmology*, **4**, 1
- Porth O., et al., 2019, *The Astrophysical Journal Supplement Series*, **243**, 26
- Porth O., Mizuno Y., Younsi Z., Fromm C. M., 2021, *MNRAS*, **502**, 2023
- Prather B., Wong G., Dhruv V., Ryan B., Dolence J., Ressler S., Gammie C., 2021, *The Journal of Open Source Software*, **6**, 3336
- Ressler S. M., White C. J., Quataert E., 2023, *MNRAS*, **521**, 4277
- Ripperda B., et al., 2019, *ApJS*, **244**, 10
- Ripperda B., Bacchini F., Philippov A. A., 2020, *ApJ*, **900**, 100
- Ripperda B., Liska M., Chatterjee K., Musoke G., Philippov A. A., Markoff S. B., Tchekhovskoy A., Younsi Z., 2022, *ApJ*, **924**, L32
- Schawinski K., Thomas D., Sarzi M., Maraston C., Kaviraj S., Joo S.-J., Yi S. K., Silk J., 2007, *Monthly Notices of the Royal Astronomical Society*, **382**, 1415
- Shakura N. I., Sunyaev R. A., 1973, *Astronomy and Astrophysics*, **24**, 337
- Silk J., Rees M. J., 1998, *Astronomy and Astrophysics*, **331**, L1
- Sironi L., Rowan M. E., Narayan R., 2021, *ApJ*, **907**, L44
- Sądowski A., Narayan R., McKinney J. C., Tchekhovskoy A., 2014, *MNRAS*, **439**, 503
- Stanzione D., West J., Evans R. T., Minyard T., Ghattas O., Panda D. K., 2020, in *Practice and Experience in Advanced Research Computing*. ACM, New York, NY, USA, pp 106–111. doi:10.1145/3311790.3396656
- Takahashi H. R., Ohsuga K., Kawashima T., Sekiguchi Y., 2016, *ApJ*, **826**, 23
- Tchekhovskoy A., Narayan R., McKinney J. C., 2011, *Monthly Notices of the Royal Astronomical Society: Letters*, **418**
- Tchekhovskoy A., McKinney J. C., Narayan R., 2012, in *Journal of Physics: Conference Series*. p. 012040
- Uzdensky D. A., Loureiro N. F., Schekochihin A. A., 2010, *Phys. Rev. Lett.*, **105**, 235002
- White C. J., Stone J. M., Quataert E., 2019, *The Astrophysical Journal*, **874**, 168
- White C. J., Mullen P. D., Jiang Y.-F., Davis S. W., Stone J. M., Morozova V., Zhang L., 2023, *ApJ*, **949**, 103
- Wong G. N., Du Y., Prather B. S., Gammie C. F., 2021, *ApJ*, **914**, 55
- Yuan F., Narayan R., 2014, *ARA&A*, **52**, 529
- Yuan F., Gan Z., Narayan R., Sadowski A., Bu D., Bai X.-N., 2015, *The Astrophysical Journal*, **804**, 101
- Zhang Y.-T., Shi J., Shu C.-W., Zhou Y., 2003, *Phys. Rev. E*, **68**, 046709
- Zhdankin V., Ripperda B., Philippov A. A., 2023, *Physical Review Research*, **5**, 043023

This paper has been typeset from a $\text{\TeX}/\text{\LaTeX}$ file prepared by the author.